

CoMFA and HQSAR studies on 6,7-dimethoxy-4-pyrrolidylquinazoline derivatives as phosphodiesterase10A inhibitors

Shridhar S. Kulkarni, Maulik R. Patel and Tanaji T. Talele*

Department of Pharmaceutical Sciences, College of Pharmacy and Allied Health Professions, St. John's University,
8000 Utopia Parkway, Jamaica, NY 11439, USA

Received 18 November 2007; revised 26 January 2008; accepted 4 February 2008
Available online 8 February 2008

Abstract—Phosphodiesterase10A (PDE10A) is an important enzyme with diverse biological actions in intracellular signaling systems, making it an emerging target for diseases such as schizophrenia, Huntington's disease, and diabetes mellitus. The objective of the current 3D QSAR study is to uncover some of the structural parameters which govern PDE10A inhibitory activity over PDE3A/B. Thus, comparative molecular field analysis (CoMFA) and hologram quantitative structure–activity relationship (HQSAR) studies were carried out on recently reported 6,7-dimethoxy-4-pyrrolidylquinazoline derivatives as PDE10A inhibitors. The best CoMFA model using atom-fit alignment approach with the bound conformation of compound **21** as the template yielded the steric parameter as a major contributor (nearly 70%) to the observed variations in biological activity. The best CoMFA model produced statistically significant results, with the cross-validated (r^2_{cv}) and conventional correlation (r^2_{ncv}) coefficients being 0.557 and 0.991, respectively, for the 21 training set compounds. Validation of the model by external set of six compounds yielded a high (0.919) predictive value. The CoMFA models of PDE10A and PDE3A/B activity were compared in order to address the selectivity issue of these inhibitors. The best HQSAR model for PDE10A was obtained with an r^2_{cv} of 0.704 and r^2_{ncv} of 0.902 using atoms, bonds, connections, chirality, donor, and acceptor as fragment distinction and default fragment size of 4–7 with three components for the **21** compounds. The HQSAR model predicted the external test-set of compounds well since a good agreement between the experimental and predicted values was verified. Taken together, the present QSAR models were found to accurately predict the PDE10A inhibitory activity of the test-set compounds and to yield reliable clues for further optimization of the quinazoline derivatives in the dataset.

© 2008 Elsevier Ltd. All rights reserved.

1. Introduction

The phosphodiesterases (PDEs) are expressed in tissues regulating a wide variety of physiological actions. Members of the PDE family differ from one another with respect to substrate affinity and specificity, primary amino acid sequence and enzymatic regulation. The PDEs play critical regulatory roles in various signal transduction pathways by regulating the duration and amplitude of signals carried by various messengers. For example, PDEs are responsible for terminating signals generated by intracellular messenger molecules such as cyclic adenosine monophosphate (cAMP) and cyclic guanosine monophosphate (cGMP) by hydrolyzing their 3'–5' phosphodiester bond. PDEs are expressed in humans

using 21 different genes and comprise 11 superfamilies.^{1,2} Previous studies have demonstrated that PDEs regulate processes such as learning and memory, vision, olfaction, platelet aggregation, aldosterone synthesis, insulin secretion, T cell activation, and penile erection.^{3–9}

PDE10A is a single member in the PDE family with dual substrate (cAMP/cGMP) property. PDE10A is of clinical interest as it is present in the central nervous system (CNS), including the cortex, hippocampus and the striatum.^{1,2} These regions of the CNS are responsible for the regulation of dopaminergic, glutamatergic, and serotonergic neuronal signal transductions. PDE10A is expressed to a large extent in the cortical and the dopaminergic region of the basal ganglia, which suggest that impaired levels of PDE10A in these regions could be related to various neurodegenerative and neuropsychiatric disorders including schizophrenia, Parkinson's disease, and Huntington's disease. The catalytic binding site of PDE10A resembles with phosphodiesterases 3 (PDE3)

Keywords: CoMFA; HQSAR; 6,7-Dimethoxy-4-pyrrolidylquinazoline; Phosphodiesterase10A.

* Corresponding author. Tel.: +1 718 990 5405; fax: +1 718 990 1877; e-mail: talelet@stjohns.edu

family, which comprises two isoforms-3A and 3B. PDE3A enzyme is predominantly expressed in the cardiovascular system, while PDE3B in the adipocytes, hepatocytes, and spermatocytes.^{10,11} In order to avoid any undesirable effects from PDE10A inhibitors on the various systems in the human body, selectivity would play a significant role. Hence, potent and selective inhibitors of PDE10A could be an instrumental tool for protection against these CNS disorders. Recently, a novel class of 6,7-dimethoxyquinazoline derivatives was reported for achieving potent and selective inhibitors of PDE10A.¹² While this manuscript was nearing completion, quinoline-based PDE10A inhibitors with insulin secretagogue activity were reported and thus demonstrate how targeting PDE10A could lead to new molecules with diverse biological actions.¹³

There has been a need for developing newer, selective, and potent inhibitors of PDE10A. A successful 3D QSAR model not only helps in better understanding of the structure–activity relationship of any class of compounds, but also ensures the researcher an in-depth analysis about the lead compounds in the further studies. Hence, we initiated CoMFA^{14,15} and HQSAR¹⁶ studies as validated tools for QSAR analysis of novel class of PDE10A inhibitors.¹² CoMFA is one of the methods of rational drug design, which has been successfully applied in our laboratory for malonyl CoA decarboxylase inhibitors,¹⁷ cytotoxic agents¹⁸ and HCV NS5B polymerase inhibitors.¹⁹ HQSAR, a 2D QSAR technique, is of particular interest since it eliminates the need for determining 3D structure, putative binding conformation, and molecular alignment. CoMFA analysis involves the alignment of molecules in a structurally and pharmacologically reasonable manner on the basis of the assumption that each compound acts via a common macromolecular target binding site. They can give critical information of the interaction between the ligand and the putative receptors. In this method, it is possible to predict the biological activity of molecules and represent the relationships between molecular properties (steric and electrostatic) and biological activity in the form of contour maps. As a result statistical data in the form of contour maps for PDE10A inhibitors can be generated to obtain an understanding of the steric and electrostatic requirements for biological activity. HQSAR model generates a molecular fingerprint of the 2D structure of the molecule and cuts it into fragments to determine its contribution towards biological activity of the molecule. HQSAR can suggest intuitionistic guidelines for structural modification during the design of novel compounds. The resulting 3D contour maps and 2D fingerprint property contributions can be useful for the future development of PDE10A inhibitors with high target site affinity and specificity.

2. Results and discussion

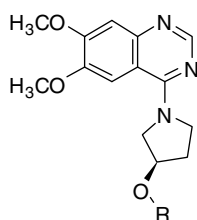
2.1. CoMFA statistical results

The training set and test-set were first evaluated for structural diversity and variations in biological activity.

The structures and biological activities of all the compounds in the training and test-set are shown in Table 1. The study was restricted to a limited set of training and test compounds since these are the only reported PDE10A inhibitors intended for CNS disorders. It is important to note that the results of Leave-One-Out (LOO), group cross-validation, test-set prediction, and high utility in designing new analogues, all point towards the robustness of the underlying QSAR model. The QSAR models are meant to be refined based on new experimental structure–activity relationship (SAR) as and when made available in the scientific literature. Thus the 3D QSAR model described here can also be refined upon availability of additional experimental SAR on PDE10A inhibitors. Two CoMFA models were generated using two different conformations of the template molecule and detailed statistical results are shown in Table 2. Model 1 was built by using geometry-optimized bound inhibitor (compound **21**) whereas model 2 was built using bound inhibitor (compound **21**) without geometry-optimization as described in Section 4.

Model 1 gave r_{cv}^2 (cross-validated r^2), r_{ncv}^2 (non-cross-validated r^2), and r_{pred}^2 (predictive r^2), values of 0.415, 0.836, and 0.307, respectively. Region-focusing showed improvement in statistical significance with r_{cv}^2 , r_{ncv}^2 , and r_{pred}^2 values of 0.538, 0.809, and 0.319, respectively. To further improve the model, field-fit alignment was used to adjust the geometry of the molecules to maximize the similarity of the steric and electrostatic fields between the template molecule and the other molecules to give the best results. The field-fit alignment resulted into the improvement of the model statistics with r_{cv}^2 , r_{ncv}^2 , and r_{pred}^2 of 0.538, 0.976, and 0.603, respectively (Table 2).

Model 2 for the same training set yielded significant r_{cv}^2 , r_{ncv}^2 , and r_{pred}^2 values of 0.557, 0.991, and 0.919, respectively. QSAR analysis performed using region-focusing gave inferior results with r_{cv}^2 , r_{ncv}^2 , and r_{pred}^2 values of 0.397, 0.728, and 0.603, respectively. Field-fit also yielded poor results with r_{cv}^2 , r_{ncv}^2 , and r_{pred}^2 values of 0.485, 0.931, and 0.816, respectively (Table 2). Even though the effect of steric and electrostatic cutoffs for the CoMFA model was studied, the corresponding statistical results were inferior to the default values (data not shown). Furthermore we have tried different charges such as Gasteiger–Huckel, Huckel, Delre, Pullman, and MMFF94 on the molecules in the dataset to evaluate the effect of charge calculation method on the statistical results. In this instance, the results were poorer than those obtained by the Gasteiger–Marsili charges for the CoMFA model (data not shown). Since the bound conformation of the template molecule **21** gave the best statistical results, further discussion is based on atom-fit alignment using model 2. Hence, we can conclude that using the bound conformation of the most potent compound **21** is the most significant method to obtain QSAR statistics. Details of the observed and predicted pK_i values derived from the training set of molecules for the best CoMFA model are given in Table 3 and graphically shown in Figure 1A.

Table 1. Structures of the training and test-set of compounds

Compound	R	PDE10A K_i (μ M)	PDE3A K_i (μ M)	PDE3B K_i (μ M)
1	2-Trifluoromethylphenyl	0.811	<0.100	>0.100
2	2-Methylphenyl	0.326	<0.100	<0.100
3	2-Methoxyphenyl	0.240	<0.100	>0.100
4	2-Cyanophenyl	0.130	<0.100	<0.100
5	4-Cyanophenyl	0.056	0.214	0.471
6	4-Trifluoromethoxyphenyl	0.185	0.739	1.820
7	4- <i>tert</i> -Butylphenyl	0.100	0.720	1.890
8	4-Ethoxyphenyl	0.054	0.161	0.328
9	3-Biphenyl	0.136	0.271	0.280
10	3-Ethoxyphenyl	0.094	0.061	0.088
11	3,4-Dimethoxyphenyl	0.067	0.121	0.260
12	5-Chloro-2-pyrimidinyl	0.044	0.162	0.332
13	3-Pyridinyl	0.128	0.302	0.748
14	4-Pyridinyl	0.112	0.226	0.685
15	2-Naphthyl	0.012	0.283	0.463
16	1-Naphthyl	0.210	0.048	0.056
17	2-(7-Methoxynaphthyl)	0.017	0.273	0.305
18	6-Quinoliny	0.012	0.104	0.201
19	7-Quinoliny	0.012	0.209	0.240
20	3-Isoquinoliny	0.019	0.151	0.196
21	2-Quinoxaliny	0.004	0.211	0.273
22 ^a	2-Chlorophenyl	0.198	<0.100	<0.100
23 ^a	3- <i>i</i> -Propylphenyl	0.171	0.370	0.474
24 ^a	5-(2,3-Dihydro-1 <i>H</i> -indenyl)	0.068	0.141	0.237
25 ^a	2-Pyridinyl	0.123	0.077	0.207
26 ^a	2-(6-Methoxynaphthyl)	0.018	0.199	0.280
27 ^a	6-(2-Methylquinoliny)	0.018	0.152	0.223

^a Test-set.

Atom-fit alignment derived from model 2 was also used to develop CoMFA model for 22 PDE3A/B inhibitors. These efforts allowed us to derive structural parameters (mainly steric fields) that govern the selectivity of these inhibitors towards PDE10A versus PDE3A/B. CoMFA model, hence, generated showed r_{cv}^2 and r_{ncv}^2 of 0.541 and 0.960 for PDE3A, while 0.526 and 0.970 for PDE3B. The experimental SAR for PDE10A versus PDE3A and 3B inhibitors is discussed in Section 2.4. The CoMFA steric fields obtained for PDE3A and 3B inhibitors were found to be contrasting with the PDE10A CoMFA steric fields and are discussed in Section 2.4.

To further assess the robustness and statistical confidence of the best CoMFA model for PDE10A, bootstrapping²⁰ analysis for 100 runs was performed (Table 2). Bootstrapping involves the generation of many new datasets from the original dataset and obtained by randomly choosing samples from the original dataset. The r_{boot}^2 value of 0.988 with standard deviation of 0.009 suggests a good consistency for the dataset. Furthermore, to investigate the stability of the model with respect to training set composition, a cross-validation analysis was used. The training set was cross-validated using

two (Leave-Half-Out) and five (leave 20% out) cross-validation groups 50 times each. The average and standard deviation (SD) values of r_{cv}^2 are shown in Table 2. The average r_{cv}^2 values for CoMFA for two and five cross-validation groups were 0.356 (SD = 0.516) and 0.539 (SD = 0.461), respectively.

2.2. HQSAR statistical results

HQSAR calculations were carried out using three distinct parameters—the fragment size, the hologram length, and the fragment type (fragment distinction). The HQSAR models were first generated using the default fragment size (4–7) combined with various fragment types and various hologram lengths. Table 4 summarizes the results for different fragment types and hologram length. With the best fragment type parameters, PLS analyses were performed to investigate if different fragment sizes could improve the statistical parameters. The HQSAR results from the different fragment sizes are summarized in Table 5. The best model was obtained using a hologram length of 61, 6 optimum number of components (o.n.c.) and Atom + Bond + Connectivity + Chirality + Donor and Acceptor as the

Table 2. Summary of CoMFA statistical results for PDE10A activity

	Model 1			Model 2		
	Manual atom fit	Field-fit	Region focusing	Manual atom fit	Field-fit	Region focusing
r_{ncv}^2 ^a	0.836	0.976	0.809	0.991	0.931	0.728
SEE ^b	0.246	0.102	0.266	0.065	0.164	0.316
F_{test}^c	45.96	123.63	38.02	315.2	76.75	24.12
r_{cv}^2 ^d	0.415	0.538	0.538	0.557	0.485	0.397
SEP ^e	0.464	0.413	0.413	0.444	0.459	0.540
r_{pred}^2 ^f	0.307	0.603	0.319	0.919	0.816	0.603
PLS components ^g	2	2	2	5	3	2
<i>Contribution</i>						
Steric	57	80	57	0.69	0.74	0.73
Electrostatic	43	20	43	0.31	0.26	0.27
r_{boot}^2 ^h	—	—	—	0.988	—	—
SEE _{boot} ⁱ	—	—	—	0.009	—	—
r_{LHO}^2 ^j	—	—	—	0.356	—	—
SD _{LHO} ^k	—	—	—	0.516	—	—
r_{scv}^2 ^l	—	—	—	0.539	—	—
SD _{scv} ^m	—	—	—	0.461	—	—

^a Correlation coefficient.^b Standard error of estimate.^c Ratio of r_{ncv}^2 explained to unexplained = $r_{\text{ncv}}^2 / (1 - r_{\text{ncv}}^2)$.^d Cross-validated correlation coefficient after Leave-One-Out procedure.^e Standard error of prediction.^f Predicted correlation coefficient for test-set of compounds.^g Optimal number of principal components.^h Average of correlation coefficient for 100 samplings using bootstrapped procedure.ⁱ Average standard error of estimate for 100 samplings using bootstrapped procedure.^j Average cross-validated correlation coefficient for 50 runs using Leave-Half-Out (LHO) group.^k Standard deviation of average cross-validated correlation coefficient for 50 runs.^l Average cross-validated correlation coefficient for 50 runs using five cross-validation groups.^m Standard deviation of average cross-validated correlation coefficient for 50 runs.**Table 3.** Observed and predicted PDE10A p*K*_i for the training and test-set from CoMFA and HQSAR models

Compound	Observed p <i>K</i> _i	CoMFA		HQSAR	
		Predicted p <i>K</i> _i	Residual p <i>K</i> _i	Predicted p <i>K</i> _i	Residual p <i>K</i> _i
1	0.10	0.14	−0.04	−0.07	0.17
2	0.49	0.54	−0.05	0.84	−0.35
3	0.62	0.63	−0.01	0.87	−0.25
4	0.89	0.85	0.04	1.04	−0.15
5	1.26	1.23	0.03	0.93	0.33
6	0.74	0.87	−0.13	0.82	−0.08
7	1.00	0.94	0.06	1.02	−0.02
8	1.27	1.24	0.03	0.95	0.32
9	0.87	0.87	0.00	0.87	0.00
10	1.03	0.96	0.07	0.99	0.04
11	1.18	1.24	−0.06	1.13	0.05
12	1.36	1.28	0.08	1.37	−0.01
13	0.90	0.90	0.00	1.13	−0.23
14	0.96	0.89	0.07	1.03	−0.07
15	1.93	1.89	0.04	1.58	0.35
16	0.68	0.73	−0.05	0.76	−0.08
17	1.77	1.79	−0.02	1.79	−0.02
18	1.93	1.92	0.01	1.97	−0.04
19	1.93	1.97	−0.04	1.99	−0.06
20	1.73	1.80	−0.07	1.70	0.03
21	2.40	2.40	0.00	2.39	0.01
22 ^a	0.71	0.74	−0.03	0.71	0.00
23 ^a	0.77	0.75	0.02	0.84	−0.07
24 ^a	1.17	1.40	−0.23	0.97	0.20
25 ^a	0.92	1.10	−0.18	1.17	−0.25
26 ^a	1.75	1.71	0.04	1.57	0.18
27 ^a	1.75	1.78	−0.03	1.83	−0.08

^a Correlation coefficient.

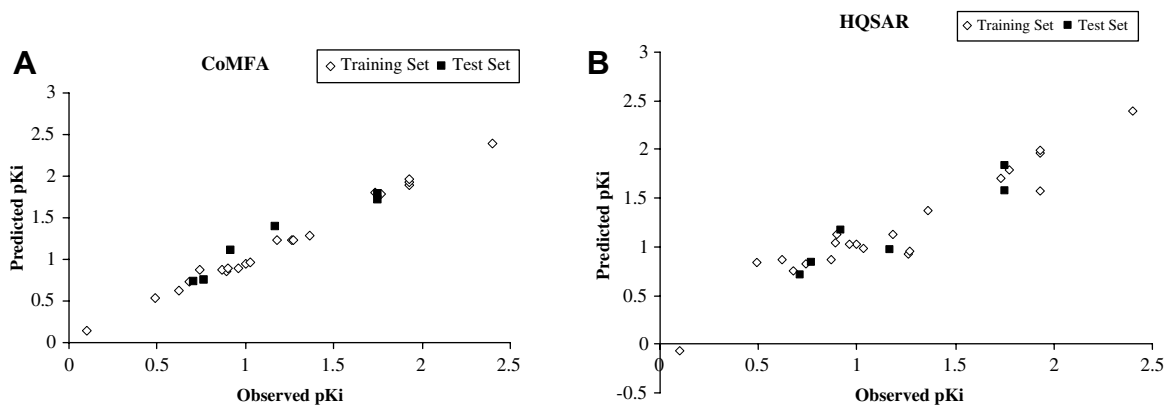


Figure 1. Plot of observed versus predicted pK_i values for the training set and test-set molecules based on CoMFA (A) and HQSAR (B) models.

Table 4. Results of HQSAR analyses for various fragment distinctions on the key statistical parameters using fragment-size default (4–7)^a

Model	Fragment	r_{cv}^2	SEP	r_{ncv}^2	SEE	HL	N
1	A/B	0.502	0.455	0.887	0.216	307	4
2	A/B/C	0.390	0.488	0.908	0.189	199	3
3	A/B/C/H	0.517	0.447	0.932	0.168	353	4
4	A/B/C/H/Ch	0.532	0.440	0.934	0.164	353	4
5	A/B/H/Ch/DA	0.622	0.423	0.985	0.084	53	5
6	A/B/H	0.604	0.418	0.935	0.169	53	2
7	A/B/C/Ch	0.398	0.485	0.912	0.186	199	3
8	A/B/DA	0.430	0.446	0.632	0.358	97	1
9	A/B/C/DA	0.564	0.413	0.933	0.162	353	3
10	A/B/H/DA	0.536	0.453	0.928	0.178	97	5
11	A/B/C/Ch/DA	0.704	0.340	0.902	0.196	59	3
12	A/B/C/H/DA	0.525	0.418	0.737	0.311	83	2
13	A/B/C/H/Ch/DA	0.604	0.433	0.989	0.073	61	6
14	A/C/H/DA	0.560	0.457	0.918	0.197	151	6
15	A/C/Ch/DA	0.446	0.457	0.775	0.296	71	3
16	A/C/DA	0.409	0.480	0.743	0.316	71	3

^a HL: hologram length, N : optimal number of components, Fragment distinction—A: atom, B: bond, C: connection, H: hydrogen, Ch: chirality, DA: donor and acceptor.

Table 5. HQSAR analysis for the influence of various fragment sizes on the key statistical parameters using the best fragment distinction (A/B/C/Ch/DA)

Fragment size	r_{cv}^2	SEP	r_{ncv}^2	SEE	HL	N
2–5	0.628	0.370	0.848	0.237	59	2
3–6	0.645	0.372	0.909	0.188	59	3
4–7	0.704	0.340	0.902	0.196	59	3
5–8	0.735	0.331	0.941	0.156	59	4
6–9	0.740	0.351	0.994	0.055	61	6
7–10	0.706	0.349	0.964	0.122	59	4
8–11	0.631	0.391	0.935	0.164	53	4

fragment type ($r_{cv}^2 = 0.740$, $r_{ncv}^2 = 0.994$). Larger fragment size was favored for improving the statistical data in the form of r_{cv}^2 and r_{ncv}^2 . However, the increment in r_{cv}^2 was not significant, only 0.036, when the fragment size changed from 2–5 to 7–10. To avoid over interpretation, we chose a model with a higher r_{cv}^2 and a smaller number of components as the final HQSAR model. This HQSAR model was built using Atom + Bond + Connectivity + Chirality + Donor and Acceptor as the fragment type and 4–7 as the fragment size, with a hologram length of 59 ($r_{cv}^2 = 0.704$, $r_{ncv}^2 = 0.902$, o.n.c. = 3) as shown in Table 5. The detailed observed pK_i and pre-

dicted pK_i values of the training set compounds for the best HQSAR model are given in Table 3 and plotted in Figure 1B. The low residual values show that the HQSAR model obtained is highly reliable and can be used to predict the biological activity of novel compounds.

2.3. Predictivity of QSAR models

The external test-set of six compounds, not included in model generation was used to evaluate the predictive ability of the training set of compounds. The predictive

correlation coefficient (r^2_{pred}) from the CoMFA model was found to be 0.919 (Table 2). The detailed observed and predicted $\text{p}K_i$ values for the test-set compounds based on the best CoMFA model are listed in Table 3 and graphically shown in Figure 1A. The high predictive ability of the HQSAR model can be judged from the r^2_{ncv} and r^2_{cv} of 0.902 and 0.704, respectively. The model predicted the test-set of compounds in terms of structural characteristics as well as the $\text{p}K_i$. The detailed observed and predicted $\text{p}K_i$ values for the test-set compounds from HQSAR model are depicted in Table 3 and graphically shown in Figure 1B. The predicted $\text{p}K_i$ residuals of the test-set for the CoMFA and HQSAR models were less than 0.3 and 0.25 log unit, respectively, which is a strong evidence that highly predictive QSAR models were obtained. Thus, the statistical agreement between the two QSAR models confirms their application in predicting the activity of untested compounds.

2.4. CoMFA contour maps and binding mode

CoMFA steric and electrostatic fields are shown in Figure 2A and B, respectively. The most potent compound **21** bound to PDE10A catalytic site (PDB ID: 2ovy),¹² is shown in Figure 2C. The steric field descriptor explained

nearly 70% of the variance in observed PDE10A inhibitory activity, and the proportion of electrostatic descriptor accounted for 30%. Therefore, the steric field had greater influence than the electrostatic field on PDE10A inhibitory activity. The green contour characterizes the regions where bulky substituents would increase the PDE10A inhibitory activity; whereas yellow contour indicates the regions where steric bulk would decrease PDE10A inhibitory activity. The contribution of the green and yellow contours was maintained as the default value of 80 and 20, respectively. The blue contour depicts the favorable sites for electropositive groups while the red contour favors the electronegative groups. The contribution of the blue and red contours was adjusted to 70 and 30, respectively.

The large green contour was found around the C-5, C-6, and C-7 positions of the quinoxaline ring of the most potent PDE10A inhibitor, compound **21** ($K_i = 0.004 \mu\text{M}$) as shown in Figure 2A. The quinoxaline ring of compound **21** has lipophilic interactions with Phe719, Ala722, and Val723 (Fig. 2C).¹² The quinazoline moiety of compound **21** is in hydrophobic contacts with the clamp residues Phe686 and Phe719 whereas the 6- and 7-OCH₃ groups were found to interact through bidentate

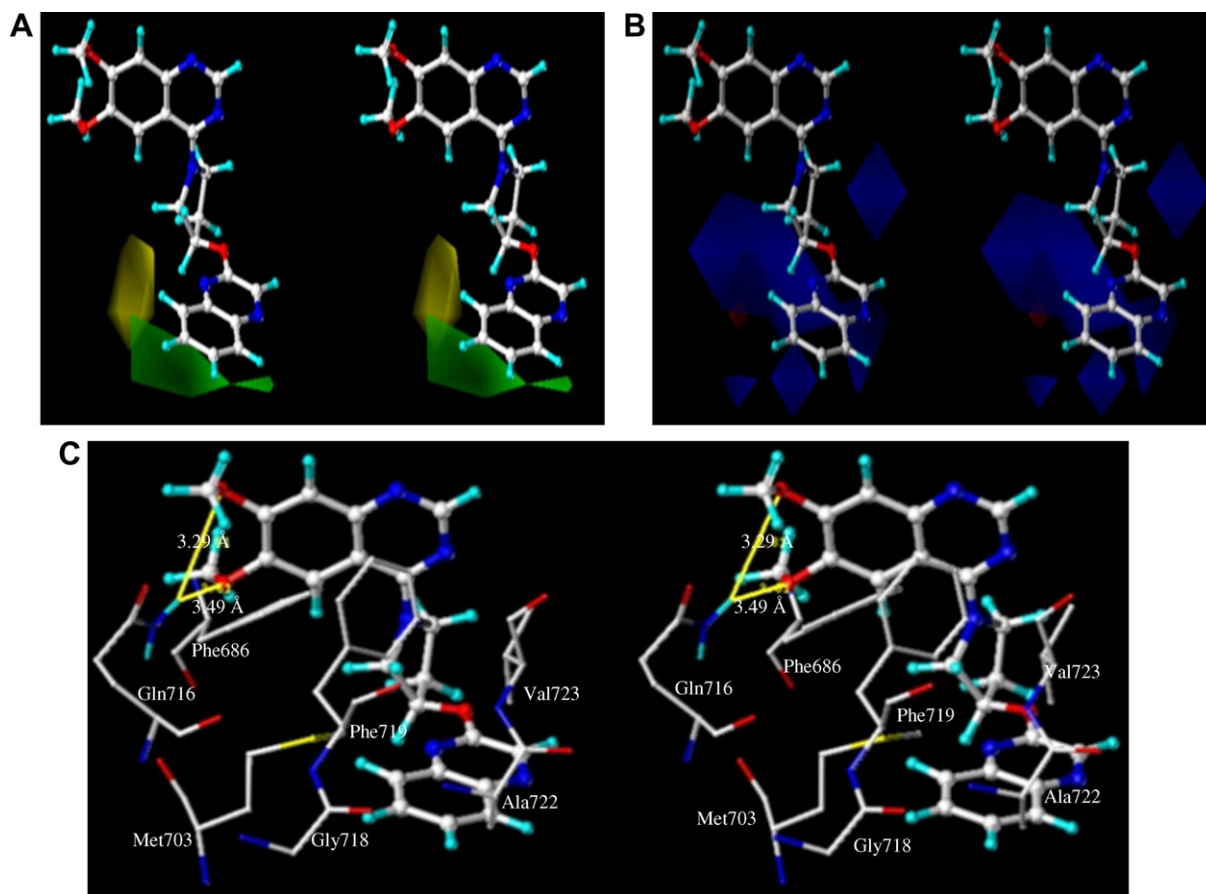


Figure 2. Stereo view of CoMFA coefficient contours (STDEV * COEFF) for steric fields (A) and electrostatic fields (B) with most potent compound **21** for PDE10A. Steric fields: green contours indicate regions where bulky groups increase activity; yellow contours indicate regions where bulky groups decrease activity. Electrostatic fields: blue contours indicate regions where electropositive groups increase activity; red contours indicate regions where electronegative groups increase activity. Stereo view of compound **21** bound within the catalytic site of PDE10A (C). Active site amino acids are shown as stick model whereas the inhibitor is shown as ball and stick model.

hydrogen bonding with the side chain $-\text{NH}_2$ of the Gln716. This may be the reason for the bicyclic compounds (e.g., compounds **15**, **17–21**, **24**, **26**, and **27**) occupying the green contour being more potent than the phenyl-substituted compounds **1–4**, **6**, **22**, and **23** and pyridinyl-substituted compounds **13**, **14**, and **25**. The green contour is in close proximity of the 4-cyano-phenyl group of compound **5** ($K_i = 0.056 \mu\text{M}$) and 4-ethoxyphenyl group of compound **8** ($K_i = 0.054 \mu\text{M}$). The methyl groups of the 4-*tert*-butyl functionality in compound **7** ($K_i = 0.1 \mu\text{M}$) occupy the green contour. The steric bulk penetrating the green contour by compounds **5**, **7**, and **8** is minimal explaining their moderate potency. The 3-biphenyl moiety of compound **9** ($K_i = 0.136 \mu\text{M}$) is seen slightly close to the green contour showing moderate potency. Further, structure-based support for the moderate potency of compound **9** is observed in the form of potential steric hindrance between the 3-biphenyl moiety in compound **9** and the side chain of Phe719. This steric hindrance explains moderate potency of compound **9**, despite being mapped near the green contour. The green contour is far from the substituted pyridinyl derivatives such as compounds **13** ($K_i = 0.128 \mu\text{M}$), **14** ($K_i = 0.112 \mu\text{M}$), and **25** ($K_i = 0.123 \mu\text{M}$), thus exhibiting moderate PDE10A potency. The green contour was occupied by the 2-naphthyl ring of compound **15** ($K_i = 0.012 \mu\text{M}$), as well as it has similar planarity to the quinoxaline ring of compound **21**. The 2-naphthyl-substituted compound **15** may be involved in similar lipophilic interactions with Phe719, Ala722, and Val723 as demonstrated for the most potent compound **21**, hence, showing significantly high potency. Similar potency of 6-quinolinyl derivative (compound **18**, $K_i = 0.012 \mu\text{M}$) and 7-quinolinyl derivative (compound **19**, $K_i = 0.012 \mu\text{M}$) may be due to the equal occupancy of sterically favorable green contour by their quinoline moiety. The 7- OCH_3 and 6- OCH_3 substituents in compounds **17** ($K_i = 0.017 \mu\text{M}$) and **26** ($K_i = 0.018 \mu\text{M}$), respectively, on the naphthyl ring, are seen near the sterically favorable green contour.

The yellow contour is seen in close proximity of the 2- CF_3 group of the least potent compound **1** ($K_i = 0.811 \mu\text{M}$). Conversely, the quinoxaline ring of the most potent compound **21** shows least proximity to the yellow contour. The compound **2** ($K_i = 0.326 \mu\text{M}$) having 2- CH_3 group shows unfavorable steric bulk near the yellow contour. The yellow contour is seen in varying distances from these groups, but their close proximity explains their low potency. The yellow contour is located in front of Met703, hence causing a distinct steric clash with the least potent 2-substituted phenyl derivatives **1–3**. The compounds **1**, **2**, and **3** with 2- CF_3 , 2- CH_3 , and 2- OCH_3 substitutions are mapped close to the $-\text{SCH}_3$ group of Met703, respectively. There is significant loss of activity in 1-naphthyl ring-substituted compound **16** ($K_i = 0.210 \mu\text{M}$), as compared to 2-naphthyl ring-substituted compound **15** ($K_i = 0.012 \mu\text{M}$). The 1-naphthyl group has close proximity to the unfavorable yellow contour similar to that of compound **1**. 1-Naphthyl group of compound **16** was mapped $\sim 2.0 \text{ \AA}$ from the side chain of Met703, thus, a possible steric hindrance within the catalytic site. Apart

from this, the compound **16** does not show any favorable hydrophobic interactions with Phe719, Ala722, and Val723 explaining significant loss of activity.

The phenyl portion of the quinoxaline moiety of compound **21** is occupied by large blue contour shown in Figure 2B, due to the presence of the electron-withdrawing pyrazinyl ring of the quinoxaline moiety. The large blue contour shows that an electron-deficient nature is important for high binding affinity. The electronegative carbonyl oxygen atom of Phe719, Val722, and Ala723 forms a favorable contact with the positively charged edge of the bicyclic aromatic ring surrounded by a blue contour. These backbone atoms show electrostatic interactions essential for differentiation in potencies of compounds with bicyclic rings such as compound **15** with substituted naphthyl ring, compounds **17** and **26** with substituted methoxynaphthyl ring, compounds **18–20** and **27** with substituted quinolinyl or isoquinolinyl ring, compound **21** with quinoxalinyl ring and compound **24** with an indenyl ring substitution. The 4-trifluoromethoxyphenyl substituted compound **6** ($K_i = 0.185 \mu\text{M}$) shows significant loss of potency, despite being mapped close to the sterically favorable green contour, because of the presence of electronegative $-\text{OCF}_3$ group in the electropositive favorable blue contour region. Compound **11** ($K_i = 0.067 \mu\text{M}$) having 3,4-dimethoxyphenyl ring substitution shows favorable electropositive methyl group of the methoxy function in the vicinity of blue contour. The methoxy groups are hence responsible for increase in potency of compound **11**, as compared to compounds **6**, **7**, **9**, and **10**. The two medium size blue contours were found to be situated on each side of the plane of the 1-naphthyl substituted compound **16** ($K_i = 0.210 \mu\text{M}$). An unsubstituted phenyl portion of the 1-naphthyl moiety of compound **16** is electronegative in nature, but being mapped closer to these two blue contours explains the significant loss of activity. The blue contour seen slightly away from pyrrolidyl ring was suggestive of electropositive nature of the ring, essential for activity. Even though the red contour was found close to the 2- CF_3 group in compound **1**, there is a steric clash of the $-\text{CF}_3$ group with side chain $-\text{SCH}_3$ of Met703. Hence, 2-substituted phenyl containing compounds such as **1–3** show least potency. Since the CoMFA models show the fields somewhat away from the molecules, it is difficult to interpret the contour maps. The partial atomic charge on carbon atom (+0.420) of the 2- CF_3 group in compound **1** is electropositive in nature due to the presence of the electron withdrawing fluoro groups, while the oxygen atom (-0.345) of the 2- OCH_3 group in compound **3** is electronegative in nature, hence, explaining the increased activity of compound **3** compared to compound **1**. The electronegative $-\text{SCH}_3$ group of Met703 is located in close proximity to the red contour. Thus, the co-localization of red and yellow contour is justified.

The development of 3D QSAR model capable of successfully predicting the crystallographic environment of PDE10A while maintaining the required inhibitor selectivity for PDE10A will be extremely helpful during the development of PDE10A inhibitors with enhanced

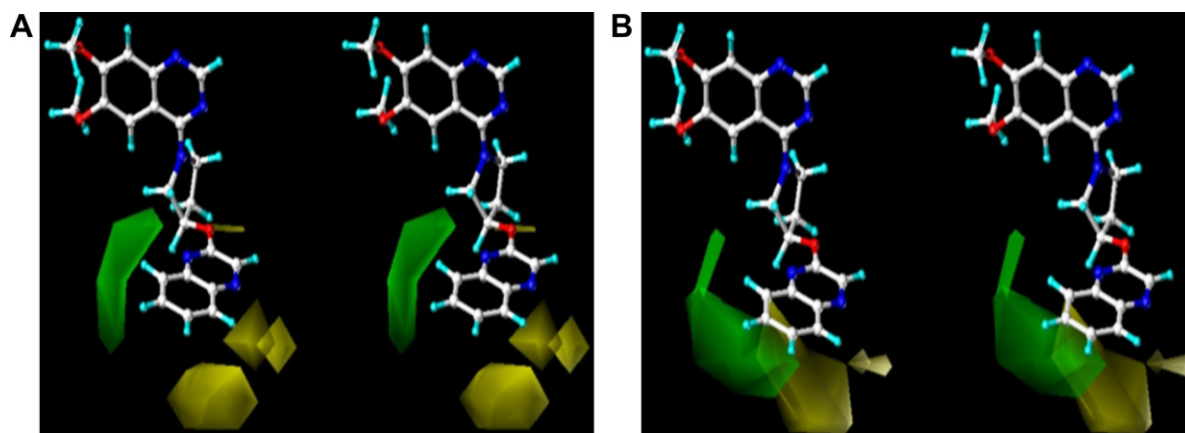


Figure 3. Stereo view of CoMFA coefficient contours (STDEV * COEFF) for steric fields for PDE3A (A) and PDE3B (B): the color scheme is the same as in Figure 2A.

potency. From the steric and electrostatic property fields generated from the CoMFA model of PDE3A/B inhibitors, only the steric property fields could be used to explain the differences in selectivity of these inhibitors for PDE10A and PDE3A/B since steric parameters are a major contributor to their inhibitory activity. Furthermore, the differences that exist between the steric CoMFA contour map of PDE10A (Fig. 2A) and that of PDE3A/B (Fig. 3A and B) can be interpreted as being the result of differences in selectivity for each isoenzyme. While in the CoMFA contour map for PDE10A the yellow area points to the steric clash in the enzyme, in the contour map of PDE3A/B the same area, shown as a large green polyhedron, corresponds to the sterically favorable site (Fig. 3A and B). Hence, finding the *ortho*-substituents of the phenyl ring of these compounds to be occupying the sterically favorable green contour in the contour maps of PDE3A and PDE3B will immediately suggest that compounds **1–4** possess a low PDE10A inhibitory activity and a modest PDE3A/B inhibitory activity. Similarly, the 1-naphthyl substituted compound **16** demonstrated a significant loss of activity towards PDE10A but a significant increase in activity towards PDE3A/B. Furthermore, in PDE3A/B a large yellow contour was found to replace the green contour in PDE10A, probably as a result of the negative effect of a sterically bulky group on inhibitory activity. Not surprisingly, compounds **15**, **17–21**, **26**, and **27** exhibited a significant inhibitory activity against PDE10A while demonstrating a moderate to low activity against PDE3A/B. The present results not only indicate that the 3D QSAR model built here for PDE10A is a working one but, in addition, that CoMFA is a useful and reliable tool for verifying the selectivity of these compounds for PDE3A/B.

2.5. HQSAR contribution map

An attractive property of HQSAR technique is that it provides straightforward clues about the individual atomic contributions to the biological activities through the use of different color codes. HQSAR color codes the individual atoms of the molecules depending upon their contribution towards the biological activity. Figure 4

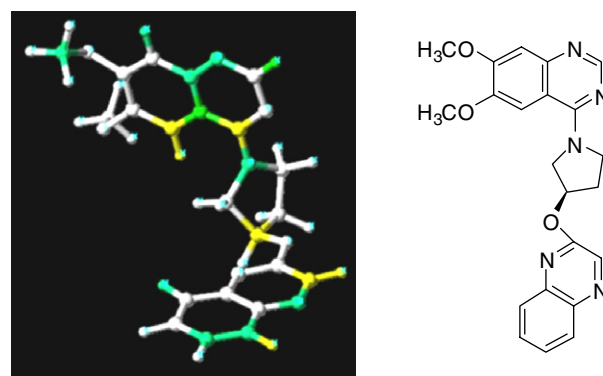


Figure 4. Individual atomic contributions for the activity of the most potent compound **21**.

depicts the individual atomic contribution of the most potent compound **21** to its molecular bioactivity. The colors at the red end of the spectrum (red, red-orange, and orange) reflect unfavorable (negative) contributions, while colors at the green end (yellow, green-blue, and green) indicate favorable (positive) contributions. Atoms with intermediate contributions are colored in white. The quinazoline ring invariant in all of the PDE10A inhibitors known until now were colored white, green, and yellow indicate positive contributions for activity, since this ring serves as a structural scaffold for holding the pharmacophoric groups in suitable orientation for maximum complementarity with the catalytic site of PDE10A. The quinoxaline ring N-atom and hydrogen atoms of the phenyl portion are shown in green color, showing maximum contribution. The pyrazinyl ring N-atoms of the quinoxaline moiety make the C-atoms of the phenyl portion more electropositive in nature, thus, explaining the presence of the blue contour over the phenyl portion of the quinoxaline ring being favorable for activity. This indicates that the position of N-atom in the quinoxaline ring is responsible for the high potency of compound **21**. One of the least potent compound **3** ($K_i = 0.240 \mu\text{M}$) shows a distinct red color methoxy group, signifying its negative contribution towards activity, which was already proven to be due to its close proximity to Met703 as well as yellow CoMFA steric contour.

The N-atom of the electronegative –CN group of compound **4** is shown as yellow in color, due to its presence close to the favorable red contour.

2.6. Design of new molecules

Ligand-based method such as CoMFA is widely used not only because it is not very computationally intensive but also because it can lead to the rapid generation of QSARs from which the biological activity of newly designed compounds can be predicted. In contrast, an accurate prediction of activity of untested compounds based on the computation of binding free energies is both complicated and lengthy. The CoMFA contour maps are a clear indicator for intuitionistic medicinal chemist for predicting novel molecules with enhanced PDE10A inhibitory activity, along with maintaining selectivity towards PDE3A/B. Also, a consistent observation made is that minor changes in the bicyclic substitutions made significant differences in activity as well as selectivity. Hence, further design of new compounds was a challenging task along with maintaining the essential selectivity between PDE10A and PDE3A/B.

Critical interpretation of the CoMFA contour maps and HQSAR results led to the identification of key structural features which could be exploited for improving the potency of the most potent reference compound **21**. Based on the blue contour maps seen in CoMFA contours, we decided to increase the electropositive nature of the ring system as well as maintain the steric bulk ensuring the new ring system has consistent hydrophobic interactions with Phe719, Ala722, and Val723. Hence, we have introduced an additional N-atom in the quinoxaline ring system making the C-atoms electropositive showing a successful increase in potency. Here, using the CoMFA model, we have designed several new quinazoline analogues with significant improvement in their pK_i values compared to the reference compound

21 as shown in Table 6. We have mainly targeted the quinoxaline moiety as it was predicted to have a significant effect on the PDE10A inhibitory activity. These newly designed compounds were included in the test-set and their activities were predicted using both CoMFA and HQSAR models. The compounds (e.g., **17**, **18**, **19**, **26**, and **27**) with either C-6 and C-7 substituents or ring-N atom at 6- and 7-position were found to be the most potent ones. Hence, electropositive substituents occupying the steric bulk favorable green contour at C-6 position along with ring-N atom at 7-position were explored.

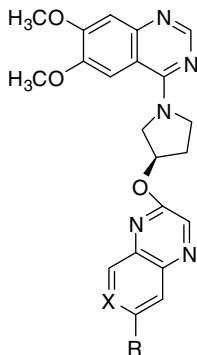
The R-substitutions in compounds **21a–21e** were mapped into the steric favorable green contour with the increasing steric bulk, hence, explaining their respective increase in activity. The electropositive charge on C-5, C-6, and C-8 of the pyridinyl ring of the azaquinoxalinyll moiety is seen to increase from compounds **21a** to **21e**. The electropositive charge on the pyridinyl portion of compounds **21d** and **21e** was found to be the same and as a result both of them showed quite identical predicted pK_i values. The predicted potencies of the ethoxy- and propoxy-substituted compounds **21d** and **21e** prove the presence of bulky substituents being favorable for activity, respectively.

3. Conclusion

In summary, the bicyclic ring substitutions around the pyrrolidylloxy position are instrumental in increasing the potency from 0.210 μM to 0.004 μM . Also, minor differences in the nature of the substitutions show significant variations in potency of these compounds, hence, implying the importance of their steric and electrostatic properties as significant parameters for explaining the observed variations in the PDE10A inhibitory activity.

Predictable and statistically significant CoMFA and HQSAR models of 6,7-dimethoxy-4-pyrrolidylquinazoline PDE10A inhibitors were obtained. A significant bootstrapped value of 0.988 with a minimal standard deviation of 0.009 was obtained for the CoMFA studies. The CoMFA model emphasizes the importance of steric descriptor field as it explained nearly 70% of the variance in PDE10A inhibitory activity. Comparison of the CoMFA steric fields for PDE10A and PDE3A/B inhibitors was conclusive towards the observed variations in selectivity for each isoenzyme. The external test-set of six compounds being predicted well explains the statistical superiority of the CoMFA and HQSAR models created and could be instrumental in exploring newer molecules that are structurally related to these PDE10A inhibitors. The predicted PDE10A inhibitory activity of the newly designed molecules was found to be quite similar based on both the CoMFA and HQSAR models. A successful HQSAR model should provide important information about what molecular fragments are directly related to the biological activity, apart from predicting the activities of the untested molecules. Together, these data would be useful for designing new compounds with potent PDE10A inhibitory activity.

Table 6. Structures and predicted PDE10A pK_i of the designed molecules **21a–21e**



Compound	R	X	CoMFA pK_i	HQSAR pK_i
21	H	C	2.40	2.39
21a	Trifluoromethoxy	N	3.09	2.41
21b	Methyl	N	3.09	2.76
21c	Methoxy	N	3.11	3.04
21d	Ethoxy	N	3.32	3.07
21e	Propoxy	N	3.32	3.09

4. Materials and methods

4.1. Data sets and biological activity

The training (21 compounds) and test (6 compounds) set used in this study comprised a series of 6,7-dimethoxy-4-pyrrolidylquinazoline derivatives, reported as potent PDE10A inhibitors.¹⁶ The biological activity data K_i in units of μM was converted to $\text{p}K_i$ and used as dependant variable. Consequently, we used 27 PDE10A inhibitors with their activities (Table 1) to establish 3D QSAR model in the present study. In addition, 3D QSAR model was developed for 22 inhibitors (all of them included in the training set) for which PDE3A/B inhibitory activity data are available (Table 1). The test-set was so divided that a representative analog was present in the training set, which concluded the study with high representative and predictive ability of the training set towards the test-set of compounds.

4.2. Molecular modeling and alignment

A Dell Precision 470n workstation with RHEL 4.0 operating system running SYBYL 7.2²¹ was used for three-dimensional structure building and molecular-modeling studies. The (*R*)-enantiomer of the training and test-set compounds was found to be more potent, hence these compounds were modeled as (*R*)-enantiomers.¹²

The molecular alignment and conformational selection are the most essential steps of 3D QSAR studies. The bioactive conformation of the most potent compound **21** was extracted from the X-ray crystal structure of the PDE10A/compound **21** complex, available in the Protein Data Bank (PDB ID: 2ovy).¹² The extracted conformation of compound **21** was used as a template molecule for alignment. The hydrogen atoms were added to the extracted conformation of the template molecule. The hybridization state of each of the atoms in crystallographic-bound inhibitor was appropriately fixed followed by subjecting it to a ‘Clean Up’ procedure available in Sketch Molecule function so as to relieve the strain from the ring atoms and bond lengths in the compound. Partial atomic charges were calculated using the Gasteiger–Marsili method.²²

Two different models were generated. Model 1 was built using the bound conformation of compound **21** as a template. Energy minimizations were performed on the template molecule with the conjugate gradient method using the Tripos force field²³ and Gasteiger–Marsili charges²² with a convergence criterion of 0.05 kcal/mol Å. The rest of the molecules were built by the Sketch Molecule function available in SYBYL using the template molecule. ‘Clean Up’ procedure was performed on all the molecules so as to relieve the strain of the rings and bonds. Model 2 was built using the crystallographic-bound inhibitor, compound **21**, as a template without subjecting to any energy minimization. The template conformation was used to build the rest of the molecules followed by ‘Clean Up’ procedure to relieve the strain if any from the newly built structural moieties.

The reference atoms of compound **21** used for the alignment were as follows: (i) C-1, C-2, C-3, C-4, and C-5 of the quinazoline ring, (ii) N-6 and C-7 of the pyrrolidine ring, and (iii) C-8 of the quinoxaline ring (Fig. 5A). The alignment of all 27 compounds using models 1 and 2 is shown in Figure 5B and C, respectively. The atom-fit alignment model was further subjected to field-fit alignment method using the SYBYL ‘field-fit’ function. To refine the model, region focusing²⁴ was also performed on the best CoMFA model. This procedure led us to six different sets of alignment models. Each alignment model was subjected to CoMFA study of PDE10A inhibitors. The atom-fit alignment model 2 was used in order to generate CoMFA models for PDE3A and PDE3B inhibitors.

4.3. CoMFA 3D QSAR models

To derive the CoMFA descriptor fields, a 3D cubic lattice with grid spacing of 2 Å in *x*, *y*, and *z* directions was created to encompass the aligned molecules. CoMFA descriptors were calculated using an sp^3 carbon probe atom with a van der Waals radius of 1.52 Å and a charge of +1.0 to generate steric (Lennard–Jones 6–12 potential) field energies and electrostatic (Coulombic potential) fields with a distance-dependent dielectric at each lattice point. The steric and electrostatic energy values were truncated at a default value of 30 kcal/mol. The CoMFA steric and electrostatic fields generated were scaled by the CoMFA standard option available in SYBYL.

A partial least-squares (PLS) approach,²⁵ an extension of multiple regression analysis, was used to derive the 3D QSAR, in which the CoMFA descriptors were used as independent variables and $\text{p}K_i$ values were dependent variables. Cross-validation with the Leave-One-Out (LOO)^{14,26} options was carried out to obtain the optimal number of components (o.n.c) to be used in the final analysis. To speed up the analysis and reduce the noise, columns with a value (σ) below 2.0 kcal/mol were filtered off. After the o.n.c was determined, a non-cross-validated analysis was performed with column filtering. The r_{cv}^2 , PRESS (the root mean predictive error sum of squares), r_{ncv}^2 , *F* value and standard error of estimate (SEE) values were computed according to the definitions in SYBYL. The cross-validated coefficient was calculated using Eq. 1:

$$r_{\text{cv}}^2 = 1 - \frac{\sum (Y_{\text{predicted}} - Y_{\text{observed}})^2}{\sum (Y_{\text{observed}} - Y_{\text{mean}})^2} \quad (1)$$

where $Y_{\text{predicted}}$, Y_{observed} and Y_{mean} are predicted, observed and mean values of the target property ($\text{p}K_i$), respectively. $\sum (Y_{\text{predicted}} - Y_{\text{observed}})^2$ are the predictive residual sum of squares (PRESS).

To further assess the robustness and the statistical confidence of the derived models, boot strapping analysis²⁰ and a number of cross-validations, for example, two and five were carried out and were confirmed by 100 runs for each cross-validation and average values of them were found. Bootstrapping involves the generation of many

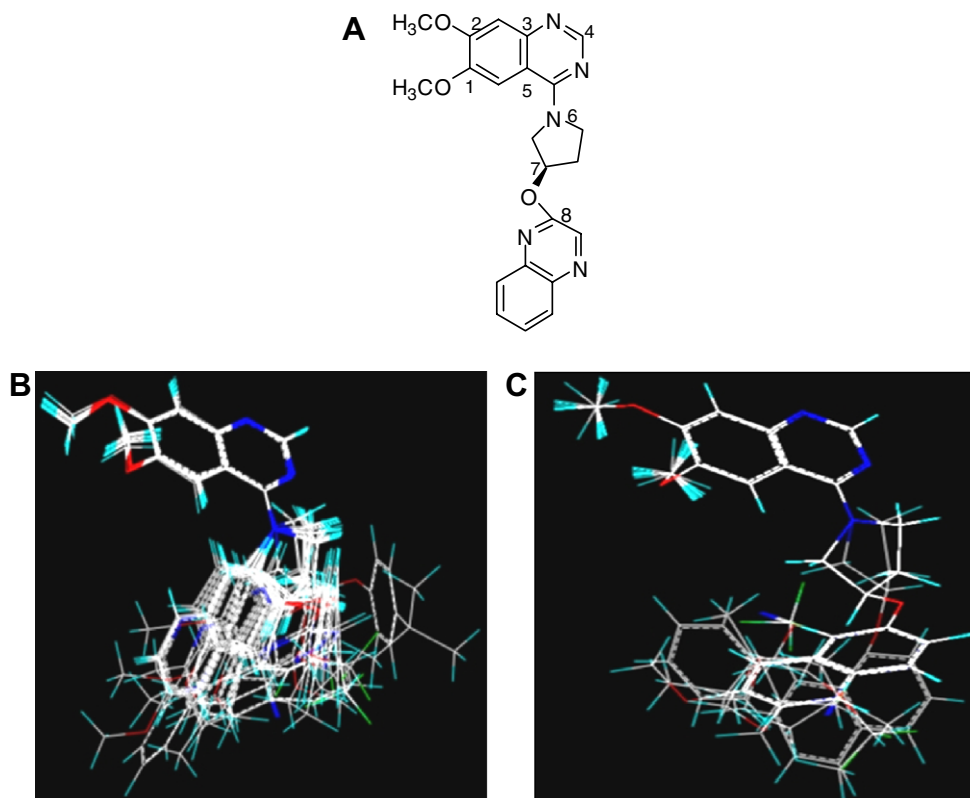


Figure 5. (A) Compound **21** used as a template for atom-based alignment. The atoms for alignment are numbered 1–8. Note that the atom-numbering does not follow IUPAC rules. Alignment of training and test-set of 27 compounds using the models 1 and 2 shown in (B) and (C), respectively.

new datasets from the original dataset and obtained by randomly choosing samples from the original dataset.

The predictive ability of each 3D QSAR model was determined from a set of six molecules not included in the model generation. The predictive correlation coefficient (r_{pred}^2), based on the test-set molecules was calculated using Eq. 2:

$$r_{\text{pred}}^2 = 1 - (\text{PRESS}/\text{SD}) \quad (2)$$

where SD is the sum of the squared deviations between the actual activities of the compounds in the test-set and the mean activity of the compounds in the training set and PRESS is the sum of the squared deviations between predicted and actual activities for every compound in the test-set. The activity of the test-set was predicted by the CoMFA model using the predict command. CoMFA coefficient maps were generated by interpolation of the pair-wise products between the PLS coefficients and the standard deviations of the corresponding CoMFA descriptor values.

4.4. HQSAR models

In HQSAR, a molecule is described as a unique string of numbers or ‘bins’ (molecular hologram). The bins represent all of the unique fragments included within a particular molecule and are assigned by a cyclic redundancy check (CRC) algorithm. All linear, branched and overlapping structure fragments were used to generate

HQSAR descriptors. The structure fragments from each original molecule consisted of a user-defined minimum and a maximum number of atoms, which are fragment-size parameters. The information in each fragment is defined by fragment distinction parameters, including atoms (A), bonds (B), connections (Con), hydrogen (H), chirality (Ch) and H donor or acceptor (DA). The generated fragments were then hashed into a fixed-length array to produce a molecular hologram. The fixed length was defined as hologram-length parameters. The HQSAR module provides 12 default hologram lengths (53, 59, 61, 71, 83, 97, 151, 199, 257, 307, 353, and 401), which are prime numbers, to minimize the possibility of fragment collision.¹⁶ The particular nature of substructure fragments generated by HQSAR and, consequently, the information contained in the resultant molecular holograms was altered by adjusting these parameters. For hologram-generation process, different combinations of these parameters were considered using the fragment-size default (4–7). The HQSAR analysis was performed by screening 12 default series of hologram length values ranging from 53 to 401 bins. The patterns of fragment counts were then related to the measured biological activity of the training set.

Acknowledgments

Support to T.T. in the form of start-up funds and resources from the College of Pharmacy of St. John’s

University are gratefully acknowledged. The authors thank Dr. Cesar Lau-Cam and Mr. Pallav Patel for critical readings of the manuscript and for helpful discussions.

References and notes

- Siuciak, J. A.; Strick, C. A. *Expert Opin. Drug Discov.* **2007**, *2*, 1001.
- Siuciak, J. A.; McCarthy, S. A.; Chapin, D. S.; Fujiwara, R. A.; James, L. C.; Williams, R. D.; Stock, J. L.; McNeish, J. D.; Strick, C. A.; Menniti, F. S.; Schmidt, C. J. *Neuropharmacology* **2006**, *51*, 374.
- Beavo, J. A. *Physiol. Rev.* **1995**, *75*, 725.
- Zhao, A. Z.; Zhao, H.; Teague, J.; Fujimoto, W.; Beavo, J. A. *Proc. Natl. Acad. Sci. USA* **1997**, *94*, 3223.
- Zhao, A. Z.; Bornfeldt, K. E.; Beavo, J. A. *J. Clin. Invest.* **1998**, *102*, 869.
- Li, L.; Yee, C.; Beavo, J. A. *Science* **1999**, *283*, 848.
- Ballard, S. A.; Gingell, C. J.; Tang, K.; Turner, L. A.; Price, M. E.; Naylor, A. M. *J. Urol.* **1998**, *159*, 2164.
- Boolell, M.; Allen, M. J.; Ballard, S. A.; Gepi-Attee, S.; Muirhead, G. J.; Naylor, A. M.; Osterloh, I. H.; Gingell, C. *Int. J. Impot. Res.* **1996**, *8*, 47.
- Chuang, A. T.; Strauss, J. D.; Murphy, R. A.; Steers, W. D. *J. Urol.* **1998**, *160*, 257.
- Shakur, Y.; Holst, L. S.; Landstrom, T. R.; Movsesian, M.; Degerman, E.; Manganiello, V. *Prog. Nucleic Acid Res. Mol. Biol.* **2001**, *66*, 241.
- Liu, H.; Maurice, D. H. *Br. J. Pharmacol.* **1998**, *125*, 1501.
- Chappie, T. A.; Humphrey, J. M.; Allen, M. P.; Estep, K. G.; Fox, C. B.; Lebel, L. A.; Liras, S.; Marr, E. S.; Menniti, F. S.; Pandit, J.; Schmidt, C. J.; Tu, M.; Williams, R. D.; Yang, F. *J. Med. Chem.* **2007**, *50*, 182.
- Cantin, L.; Magunson, S.; Gunn, D.; Barucci, N.; Breuhaus, M.; Bullock, W. H.; Burke, J.; Claus, T. H.; Daly, M.; DeCarr, L.; Gore-Willse, A.; Hoover-Litty, H.; Kumarasinghe, E. S.; Li, Y.; Liang, S. X.; Livingston, J. N.; Lowinger, T.; MacDougall, M.; Ogutu, H. O.; Olague, A.; Ott-morgan, R.; Schoenleber, R. W.; Tersteegen, A.; Wickens, P.; Zhang, Z.; Zhu, J.; Sweet, L. J. *Bioorg. Med. Chem. Lett.* **2007**, *17*, 2869.
- Cramer, R. D., III; Patterson, D. E.; Bunce, J. D. *J. Am. Chem. Soc.* **1988**, *110*, 5959.
- Cramer, R. D., III; Bunce, J. D.; Patterson, D. E.; Frank, I. E. *Quant. Struct.-Act. Relat.* **1988**, *7*, 18.
- HQSAR™ Manual SYBYL 7.2, Tripos 1699 South Hanley Road, St. Louis, Missouri, 63144.
- Patel, M. R.; Talele, T. T. *Bioorg. Med. Chem.* **2007**, *15*, 4470.
- Patel, M. R.; Dimmock, J. R.; Talele, T. T. *J. Chem. Inf. Model.* **2007**, *47*, 2110.
- Patel, P. D.; Patel, M. R.; Kaushik-Basu, N.; Talele, T. T. *J. Chem. Inf. Model.* **2008**, *48*, 42.
- Vong, R.; Geladi, P.; Wold, S.; Esbensen, K. *J. Chemom.* **1988**, *2*, 281.
- SYBYL 7.2, Tripos Inc., 1699 South Hanley Road, St. Louis, Missouri, 63144.
- Gasteiger, J.; Marsili, M. *Tetrahedron* **1980**, *36*, 3219.
- Clark, M.; Cramer, R. D., III; Van Opdenbosch, N. *J. Comput. Chem.* **1989**, *10*, 982.
- Lindgren, F.; Geladi, P.; Rannar, S.; Wold, S. *J. Chemom.* **1994**, *8*, 349.
- Wold, S.; Albano, C.; Dunn, W. J.; Edlund, U.; Esbensen, K.; Geladi, P.; Hellberg, S.; Lindburg, W.; Sjostorm, M. In *Chemometrics*; Kowalski, B., Ed.; Reidel: Dordrecht, The Netherlands, 1984; p 17.
- Wold, S. *Technometrics* **1978**, *4*, 397.